Computational Aero-Acoustic Using High-order Finite-Difference Schemes

Zhu, Wei Jun; Shen, Wen Zhong; Sørensen, Jens Nørkær

Published in:
Journal of Physics: Conference Series (Online)

Link to article, DOI:
10.1088/1742-6596/75/1/012084

Publication date:
2007

Document Version
Publisher's PDF, also known as Version of record

Computational Aero-Acoustic Using High-order Finite-Difference Schemes

2007 J. Phys.: Conf. Ser. 75 012084

(http://iopscience.iop.org/1742-6596/75/1/012084)

Journal of Physics: Conference Series **75** (2007) 012084 doi:10.1088/1742-6596/75/1/012084

Computational Aero-Acoustic Using High-order Finite-Difference Schemes

Wei Jun Zhu, Wen Zhong Shen and Jens Nørkær Sørensen

Department of Mechanical Engineering, Fluid Mechanics Section, Building 403, Technical University of Denmark, DK-2800 Lyngby, Denmark

E-mail: wjz@mek.dtu.dk

Abstract. In this paper, a high-order technique to accurately predict flow-generated noise is introduced. The technique consists of solving the viscous incompressible flow equations and inviscid acoustic equations using a incompressible/compressible splitting technique. The incompressible flow equations are solved using the in-house flow solver EllipSys2D/3D which is a second-order finite volume code. The acoustic solution is found by solving the acoustic equations using high-order finite difference schemes. The incompressible flow equations and the acoustic equations are solved at the same time levels where the pressure and the velocities obtained from the incompressible equations form the input to the acoustic equations. To achieve low dissipation and dispersion errors, either Dispersion-Relation-Preserving (DRP) schemes or optimized compact finite difference schemes are used for spatial discretizations of the acoustic equations. The classical fourth-order Runge-Kutta time scheme is applied to the acoustic equations for time discretization.

1. Introduction

Sound is generated from many fundamental physical phenomena where the flow induced noise is of our interest in the present paper. It is the unsteady part of the flow that is responsible for flow induced noise since steady flows never generate noise. Therefore, the prediction of sound generation is a combined task of flow and acoustic simulations, the discipline is usually referred to Computational Aero-acoustic (CAA).

The aeroacoustic computation of flow generated noise was pioneered by Lighthill [1] in the 1950th. Soon after that, Lighthill's equation, the acoustic analogy, became widely used. The acoustic analogy is applied for flow generated noise in many situations. Examples include noise from wind turbines, aircrafts, helicopter rotors, turbo machines etc. Improvements of Lighthill's acoustic equation are still going on and much effort is still made to generalize the theoretical description. Among those, Curle [2] extended the theory by including the influence of static boundaries. Subsequently, Ffowcs Williams et al. [3] extended it further by including the influence of boundaries in arbitrary motion. In all the approaches, the key issue is to compute the sound sources generated by the flow that relates exactly to integrals of surface and volume source terms. These source terms are obtained by solving the incompressible Navier-Stokes equations in the near-field. Once the source terms are known, the acoustic far-field can be solved by using the acoustic analogy.

The most accurate way of simulating aerodynamically generated noise is to use Direct Numerical Simulation (DNS) where both fluid flow and sound are obtained directly from solving the compressible Navier-Stokes (NS) equations. With this method, it is possible to accurately predict near-field sound generation as well as far-field propagation. To solve the problem, a very fine mesh and highly accurate schemes both in space and time are needed. The method is straight forward, however, studies using DNS to simulate aeroacoustic are very few as compared to other methods since DNS requires a large amount of computer resource.

For low speed flow, a different method called incompressible/compressible splitting method was proposed by Hardin and Pope [4] in 1994. Shen and Sørensen [5] remedied the original splitting technique by changing slightly the basic decomposition of variables. The decomposition technique proposed by Shen and Sørensen is used in the present work. The first part of the splitting approach is the viscous flow part which is governed by the incompressible Navier-Stokes equations. The solutions obtained from the incompressible flow solver are used for the second part of the calculation that is the acoustic equations or the perturbed compressible equations. Under assumptions of low Mach number flow, the perturbed quantities represent the difference between the compressible flow and the incompressible flow. Therefore, the perturbed variables are the unknowns in the acoustic equations while all incompressible quantities are known at each time level. The modified splitting method has been applied by Shen and Sørensen [6,7] for both laminar and turbulent flow past circular cylinders and airfoils using a second-order finite volume method for flow and acoustic computations. The results obtained from previous computations are encouraging. However, a more effective and convenient method is needed for near field acoustic simulation at low Mach numbers. As an extension to previous work, in this paper, high-order finite difference schemes are used to solve the acoustic equations. The use of high-order schemes is due to the large disparity between the length and time scales of flow and acoustics. The 4^{th}-order explicit Dispersion-Relation-Preserving (DRP) [8] scheme was developed by Tam and Webb which is a wave number based scheme. Using the same strategy of DRP scheme and apply on the original high-order compact finite difference schemes of Lele [9], Kim et al. [10] derived an optimized implicit finite difference compact scheme. Both the high-order DRP schemes and the optimized compact schemes have the characteristic of low dissipation and dispersion error which are needed for wave problems. These two type of schemes are used to solve acoustic equations.

The paper is structured as follows: In section 2 the flow and acoustic governing equations are shown. In section 3 numerical features are introduced, such as high-order discretization and boundary treatments. In Section 4.1 a benchmark problem of acoustic scattering from a circular cylinder is used as a validation case. Noise generation from a turbulent flow past a NACA airfoil is shown in Section 4.2.

2. Governing equations

At low Mach numbers, the feed back of the acoustic field to incompressible flow field is neglected. Therefore the flow solution can be determined by solving the incompressible NS equations

$$\frac{\partial U_i}{\partial t}+\frac{\partial (U_i U_j)}{\partial x_j}=-\frac{1}{\rho_0}\frac{\partial (P+2/3\rho_0 k)}{\partial x_i}+\frac{\partial}{\partial x_j}\left[(\nu+\nu_t)\left(\frac{\partial U_i}{\partial x_j}+\frac{\partial U_j}{\partial x_i}\right)\right]$$
$$\frac{\partial U_i}{\partial x_i}=0 \qquad (1)$$

where P, ρ_0 and U_j are the incompressible pressure, the ambient density and the velocity components, respectively, ν_t is the turbulent viscosity and k is the turbulent kinetic energy obtained from a turbulence model.

The formulation of the acoustic equations was originally proposed by Hardin and Pope and further developed by Shen and Sørensen. For more details the reader is referred to [4,5]. By neglecting the viscous terms, the acoustic equations are in conservative form written as

$$\frac{\partial Q}{\partial t}+\frac{\partial E}{\partial x}+\frac{\partial F}{\partial y}+\frac{\partial G}{\partial z}=S\,, \tag{2}$$

where *Q, E, F, G, S* are given as

$$Q=\begin{pmatrix}\rho'\\ \rho u'+\rho' U\\ \rho v'+\rho' V\\ \rho w'+\rho' W\\ p'\end{pmatrix}, E=\begin{pmatrix}\rho u'+\rho' U\\ \rho(2Uu'+u'^2)+\rho' U^2+p'\\ \rho(Vu'+Uv'+u'v')+\rho' UV\\ \rho(Wu'+Uw'+u'w')+\rho' UW\\ c^2(\rho u'+\rho' U)\end{pmatrix}, F=\begin{pmatrix}\rho v'+\rho' V\\ \rho(Vu'+Uv'+u'v')+\rho' UV\\ \rho(2Vv'+v'^2)+\rho' V^2+p'\\ \rho(Vw'+Wv'+v'w')+\rho' VW\\ c^2(\rho v'+\rho' V)\end{pmatrix},$$
$$G=\begin{pmatrix}\rho w'+\rho' W\\ \rho(Wu'+Uw'+u'w')+\rho' UW\\ \rho(Wv'+Vw'+v'w')+\rho' VW\\ \rho(2Ww'+w'^2)+\rho' W^2+p'\\ c^2(\rho w'+\rho' W)\end{pmatrix}, S=\begin{pmatrix}0\\ 0\\ 0\\ 0\\ -\dfrac{\partial P}{\partial t}\end{pmatrix}. \tag{3}$$

In the matrices the quantities with superscript indicate acoustic variables and capital letters define flow variables. The acoustic computation can be started at any time after the flow computation is started. The flow parameters define the input to the acoustic equations and the acoustic equations are solved at the same time level. In order to solve the governing equations in a curvilinear coordinates the governing equations are transformed into a general curvilinear coordinate system.

3. Numerical features

3.1. Time discretization

For the time discretization, a four-step Runge-Kutta method is given by

Step 1: $q^{(1)}=q^n+\frac{\Delta t}{2}R^n$

Step 2: $q^{(2)}=q^n+\frac{\Delta t}{2}R^{(1)}$

Step 3: $q^{(3)}=q^n+\Delta t R^{(2)}$

Step 4: $q^{(4)}=q^n+\frac{\Delta t}{6}(R^{(n)}+2R^{(1)}+2R^{(2)}+R^{(3)})$

where q represents the acoustic variables *u, v, w, p,* ρ, and $R^{(\,)}=\partial q^{(\,)}/\partial t$. At each *step*, $\partial q^{(\,)}/\partial t$ is found from the acoustic equations (2) and (3) by using q values obtained at previous *step*.

3.2. Spatial discretization

The DRP schemes were developed by Tam and Webb [8] in 1993. The spatial derivatives with finite difference schemes are optimized in the wave-number space to have more satisfied dispersive properties. The methodology is summarized in brief in the following.

A standard finite difference schemes can be written as the equation below

$$\frac{\partial f}{\partial x}(x)\approx\frac{1}{\Delta x}\sum_{j=-N}^{M}a_j f(x+j\Delta x) \tag{4}$$

where M=N represents centralized finite difference schemes. The stencil width of the scheme is M+N+1 and the order of accuracy is M+N.

By using Fourier transformation of *f(x)*

$$\widetilde{f}(\alpha) = \frac{1}{2\pi}\int_{-\infty}^{\infty} f(x)e^{-i\alpha x}dx\,, \tag{5}$$

we have,

$$i\alpha\widetilde{f} \cong \frac{1}{\Delta x}\left[\sum_{j=-N}^{M} a_j e^{ij\alpha\Delta x}\right]\widetilde{f}\,. \tag{6}$$

After a small arrangement, we have

$$\overline{\alpha}\Delta x = -i\sum_{j=-N}^{M} a_j e^{ij\alpha\Delta x}\,. \tag{7}$$

In this equation $\overline{\alpha}\Delta x$ is the modified wave number which is a function of the exact wave number $\alpha\Delta x$ on the right hand side. One of the key issues of CAA is that the numerical solution in the resolvable wave number range should be as close as possible to the exact solution. In other word, the physical shape of a wave should be well represented by numerical simulations. Thus, $\overline{\alpha}\Delta x$ should be as close as possible to $\alpha\Delta x$. This is done by minimization of the error between $\overline{\alpha}\Delta x$ and $\alpha\Delta x$.

$$E = \int_0^{\pi} \left|\alpha\Delta x - \overline{\alpha}\Delta x\right|^2 d(\alpha\Delta x) \tag{8}$$

To minimize *E* one can take the derivative of *E* with respect to one of the unknown coefficients a_j of the scheme and force the derivative to be zero.

$$\frac{\partial E}{\partial a_j} = 0\,,\ j \in [\text{-N,M}] \tag{9}$$

To find all the coefficients a_j, additional equations are obtained by Taylor expansion of the original finite difference equation and equating the terms to match the desired order of accuracy M+N-2. After using the relation, we have one free coefficient a_j left which is used to minimize the integral error *E*.

Compact finite difference schemes have spectral-like resolution, as shown by Lele [9] in 1992. The compact difference schemes are implicit in nature and computationally slightly more expensive than explicit schemes. However the schemes have shown a higher ability to apply for DNS and CAA. The optimized compact finite difference schemes were proposed by Kim and Lee [10] a few years later than the DRP schemes. The optimized compact finite difference schemes combine DRP technique and compact finite schemes. The optimized schemes are formulated in the same way as the original compact schemes as shown below.

$$\beta f'_{i-2} + \alpha f'_{i-1} + f'_i + \alpha f'_{i+1} + \beta f'_{i+2} = a\frac{f_{i+1}-f_{i-1}}{2\Delta x} + b\frac{f_{i+2}-f_{i-2}}{4\Delta x} + c\frac{f_{i+3}-f_{i-3}}{6\Delta x} \tag{10}$$

The coefficients of (10) are obtained in a similar way as the DRP schemes are derived. The modified wave number is calculated in (11) and the integral error is given in (12) where *W* is a weighting function to make it integratable.

$$\omega'\Delta x = \frac{a\sin(\omega\Delta x) + \frac{b}{2}\sin(2\omega\Delta x) + \frac{c}{2}\sin(3\omega\Delta x)}{1 + 2\alpha\cos(\omega\Delta x) + 2\beta\cos(2\omega\Delta x)} \tag{11}$$

$$E = \int_0^{r\pi} \left|\omega\Delta x - \omega'\Delta x\right|^2 W(\omega\Delta x)d(\omega\Delta x) \tag{12}$$

3.3. Boundary conditions

Boundary conditions play an important role in CAA. Any wave reflected by the farfield boundary will travel back to the inner domain and affect the other waves inside for a long time period. At far fields, the radiation boundary conditions of Tam and Webb [8] are used. The radiation boundary conditions for outgoing acoustic waves are based on the asymptotic solution, shown in (13).

$$\left[\frac{\partial}{\partial t}+V(\theta)\frac{\partial}{\partial r}+\frac{\partial V(\theta)}{2r}\right]\begin{pmatrix}\rho'\\ \mathbf{u}'\\ p'\end{pmatrix}=0 \tag{13}$$

where $V(\theta)$ is the group velocity, ρ', p' and $\mathbf{u}'$ are acoustic density, pressure and velocities, respectively. The boundary schemes used at farfield are backward schemes as shown in Figure 1. The radiation boundary condition is used together with the backward stencils.

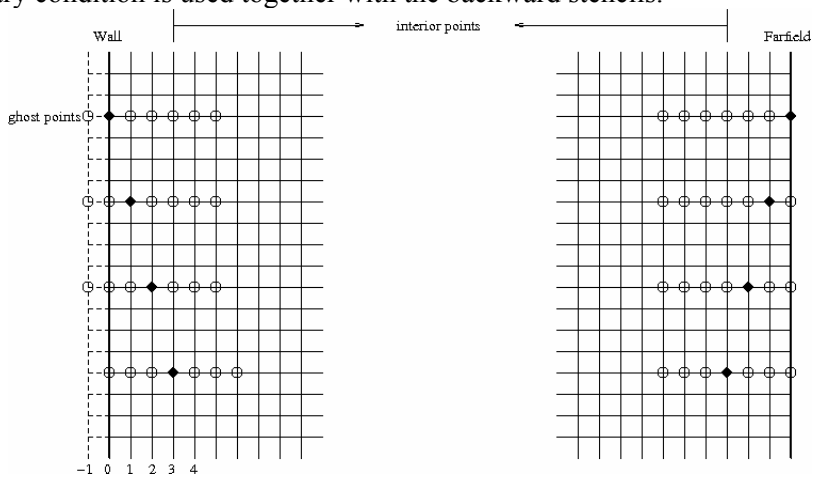

Figure 1 Seven-point stencils used in interior, wall and farfield regions.

Inviscid wall boundary conditions are employed at solid wall boundaries where the normal component of velocity is set equal to zero. For explicit DRP schemes, backward DRP schemes and one ghost point inside the wall surface are used whenever the computational stencils extend inside the wall, see Figure 1. For compact schemes, for example a tridiagonal 6th-order optimized compact finite difference scheme, compact boundary closures must be provided with three points at each end of the computational domain. A series of compact fourth- and sixth-order schemes are analysed to ensure the stability. A detailed study on boundary treatments of compact schemes is given by Carpenter et al. [11]. In our numerical code, 4th-order compact boundary schemes are provided at the first layer and 5th-order compact boundary schemes are provided at the second and third layers. This can be shown more clearly by denoting the nomenclature (4th, 5th, 5th –6th– 5th, 5th, 4th) where the –6th– denotes the inner scheme that is of 6th-order accuracy. The boundary schemes are shown below.

Fourth-order closure at $j=1$

$$6f_1'+18f_2'=\frac{1}{\Delta x}(-17f_1+9f_2+9f_3-f_4)\,. \tag{14}$$

Fifth-order closure at $j=2,3$

$$\begin{aligned}3f_1'+18f_2'+9f_3'&=\frac{1}{\Delta x}(-10f_1-9f_2+18f_3+f_4)\\ 3f_2'+18f_3'+9f_4'&=\frac{1}{\Delta x}(-10f_2-9f_3+18f_4+f_5).\end{aligned} \tag{15}$$

3.4. Filter schemes

Both DRP and optimized compact schemes are central finite difference schemes, numerical oscillations are not dissipated with these symmetric schemes. One way to ensure the numerical stability is to apply filter schemes. High-order filter schemes proposed by Bogey and Bailly [12] are used to remove spurious short waves while not affecting the long waves. A filter stencil contains 2N+1 points and the filter equation is written as

$$u_f(x_0) = u(x_0) - \sigma D(x_0) \tag{16}$$

with

$$D(x_0) = \sum_{j=-N}^{N} d_j u(x_0 + j\Delta x) \tag{17}$$

where u_f is the filtered value and u is the original value. The coefficients d_j are such as $d_j=d_{-j}$ ensuring no dispersion and σ is a damping coefficient taking values between 0 and 1. In the present study, a 9-point optimized selective filter is used together with high-order schemes. All acoustic variables are filtered after the 4th-stage of the Runge-Kutta time integration.

4. Results and discussions

4.1. Acoustic scattering from a circular cylinder

A test case is selected from the second computational aeroacoustic workshop on benchmark problems [13]. The problem 2 in Category 1 was selected which is a simplified model in which the sound source generated by a propeller is scattered off by the fuselage of an aircraft. The task is to find the time history of acoustic pressure fluctuation $p(t)$ at three points, A ($r = 5$, $\theta = 90^o$), B($r = 5$, $\theta = 135^o$) and C ($r = 5$, $\theta = 180^o$).

The circular cylinder has a radius $r = 0.5$ and is located at the center of computational domain. The numerical calculation is carried out in a domain between two concentrical cylinders of $r = 0.5$ and $r = 10.5$. Since the problem is symmetric, only half of the computational plane ($\theta = 0 \rightarrow \pi$) is used instead of using the entire azimuthal plane. The computational grid contains 201×201 cells which are equidistant both in the radial and azimuthal direction. This is also a good case to test both wall and far field boundary conditions on a curvilinear mesh.

At time T = 0, the initial pressure pulse is located at $x = 4$, $y = 0$ and generated by (18).

$$p(x, y, 0) = \exp\left[-\ln(2) \frac{(x-4)^2 + y^2}{(0.2)^2} \right] \tag{18}$$

The initial velocities v_r and v_θ are set equal to zero.

The linearized Euler equation in a polar frame is written as

$$\frac{\partial}{\partial t}\begin{pmatrix} v_r \\ v_\theta \\ p \end{pmatrix} + \frac{\partial}{\partial r}\begin{pmatrix} p \\ 0 \\ v_r \end{pmatrix} + \frac{1}{r}\frac{\partial}{\partial \theta}\begin{pmatrix} 0 \\ p \\ v_\theta \end{pmatrix} + \frac{1}{r}\begin{pmatrix} 0 \\ 0 \\ v_r \end{pmatrix} = 0 \tag{19}$$

In this example, the spatial derivatives are calculated using the 4th-order DRP scheme with seven-point stencils. Therefore, at farfield and wall boundaries various seven-point backward difference DRP schemes are applied. At farfield the acoustic radiation condition is used as shown in (20).

$$\frac{\partial}{\partial t}\begin{pmatrix} v_r \\ v_\theta \\ p \end{pmatrix} + \frac{\partial}{\partial r}\begin{pmatrix} v_r \\ v_\theta \\ p \end{pmatrix} + \frac{1}{2r}\begin{pmatrix} v_r \\ v_\theta \\ p \end{pmatrix} = 0 \tag{20}$$

It is shown in Figure 1 that derivatives of the first three layers at farfield boundary are calculated using backward schemes. Acoustic radiation boundary conditions are applied at those three layers and the equations are solved at each stage of the 4th-order Runge-Kutta time integration.

No-slip boundary conditions are applied on wall boundaries where the normal velocity on the wall is put equal to zero. The normal derivatives $\partial v_r / \partial r$ at the first three layers are computed in the same way as the farfield where only grid points lying inside the physical domain are used. For the normal derivatives of p near the wall boundary (Figure 1), the computational domain is extended to one ghost point inside the wall. The backward stencils are used to find $\partial p/\partial r$ and pressure values from the ghost points are included in the backward stencil. The value of the ghost pressure is calculated using the condition that the pressure gradient is zero on the wall.

At the plane $\theta = 0$ and $\theta = \pi$, symmetric conditions are used

$$\begin{aligned} \frac{\partial v_r}{\partial \theta} &= 0, \\ v_\theta &= 0, \\ \frac{\partial p}{\partial \theta} &= 0. \end{aligned} \tag{21}$$

The derivatives at the symmetric plane are calculated as interior points with

$$\begin{pmatrix} v_r \\ v_\theta \\ p \end{pmatrix}_{-j} = \begin{pmatrix} v_r \\ -v_\theta \\ p \end{pmatrix}_{+j} . \tag{22}$$

Results for this problem are given in Figures 2 and 3. Figure 2 shows snapshots of the pressure contour at different times. At time $T = 4$ the large wave front reaches the cylinder surface and a small reflected wave can be seen near the cylinder. At $T = 6$ the third wave front is observed near the cylinder which is generated when the initial wave propagates over the cylinder. At $T = 8$ the initial pulse has already reached the out boundary and a smooth transition towards outside is seen as expected.

In Figure 3 time history data of the pressure are compared to exact data [13] at three locations. From the plot, good agreements are seen between the simulated and the exact data at all three test points.

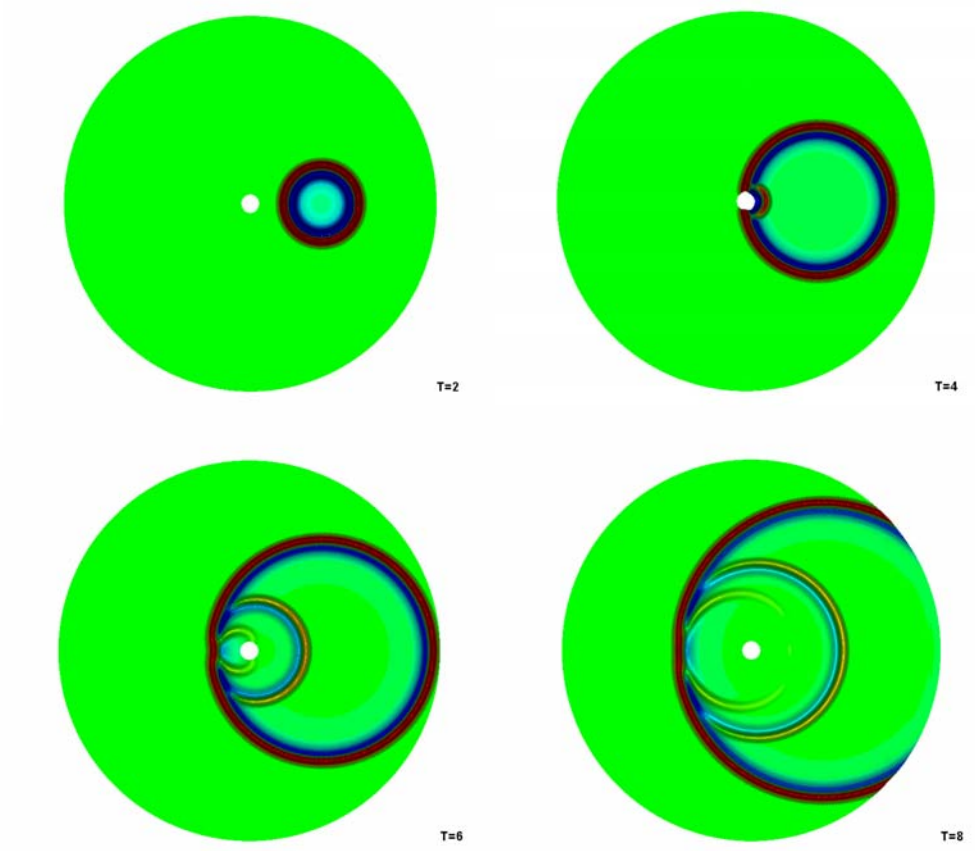

Figure 2. Instantaneous acoustic pressure contours at time T = 2, 4, 6 and 8.

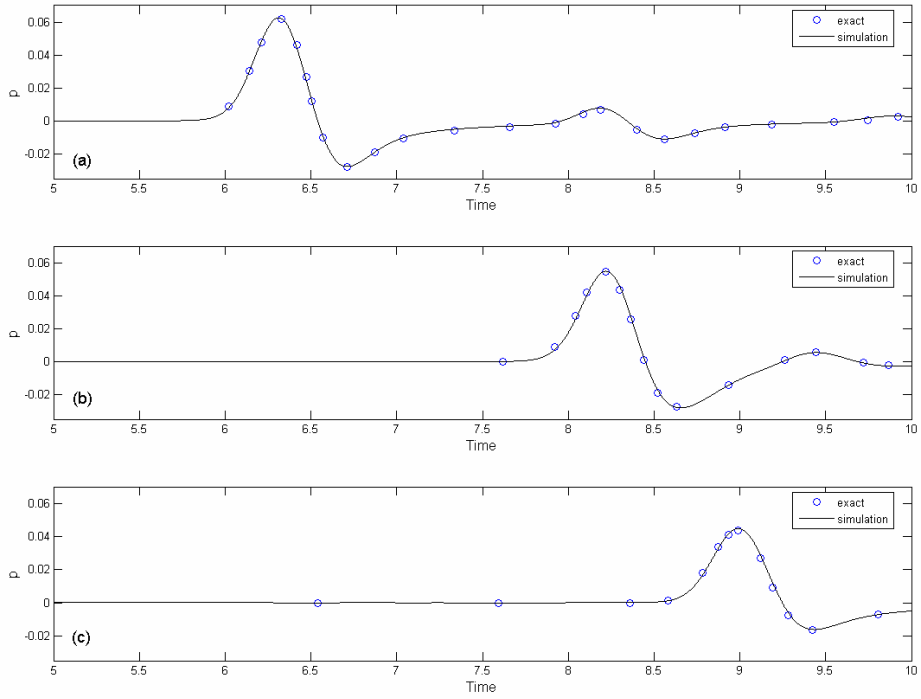

Figure 3. Comparisons between computed and exact data. (a) Time history of acoustic pressure at point A ($r = 5$, $\theta = 90^o$). (b) Time history of acoustic pressure at point B ($r = 5$, $\theta = 135^o$). (c) Time history of acoustic pressure at point C ($r = 5$, $\theta = 180^o$).

4.2. Flow and acoustic computation of a 2D NACA 0012 airfoil

In this section, flow and acoustic fields around a 2D NACA 0012 airfoil at a Reynolds number of 10^5 are simulated. The 2nd order finite volume code EllipSys by Michelsen [14] and Sørenson [15] is used for flow simulation. Turbulence structures are modeled with a Sub-Grid Scale (SGS) model for Large-eddy Simulation (LES). For acoustic computations, the 6th-order optimized compact central-difference interior scheme is used together with asymmetrically closed boundary schemes. Time calculation is advanced by the 4th-order Runge-Kutta method. The computational domain extends 25 chord length radially away from the airfoil. A 2D structured body-fitted O-mesh is generated with 24 blocks of 64×64 mesh points in each block. The computational grids in the radial direction are exponentially clustered on the airfoil surface. The numerical oscillations generated by high-order finite-difference schemes are suppressed by using the 9th -order filter schemes [12]. The filter schemes successfully damp out high frequency modes which are essentially important for convergence.

The computed sound pressure is plotted in Figure 4 at an angle of attack of 5º and a Mach number of 0.2. Figure 4(a) is a 3-dimensional view of the acoustic pressure field near the airfoil. The inflow direction is the positive x-direction and the airfoil is located at the center. It is not surprising to see that strong acoustic fluctuations take place on the airfoil surface and in the wake. A number of positive and negative acoustic pressure sources are located along the pressure and suction sides of the airfoil surface. Acoustic waves are generated in such a way that positive and negative fluctuating pressures switch their signs periodically, corresponding to vortex shedding. The sources act as dipoles and produce waves with different frequencies. Figure 4(b) is a plot of contour lines of the acoustic pressure waves in a range of ±0.015. Three receiver points P1, P2 and P3 are depicted in the plot where time history data are recorded.

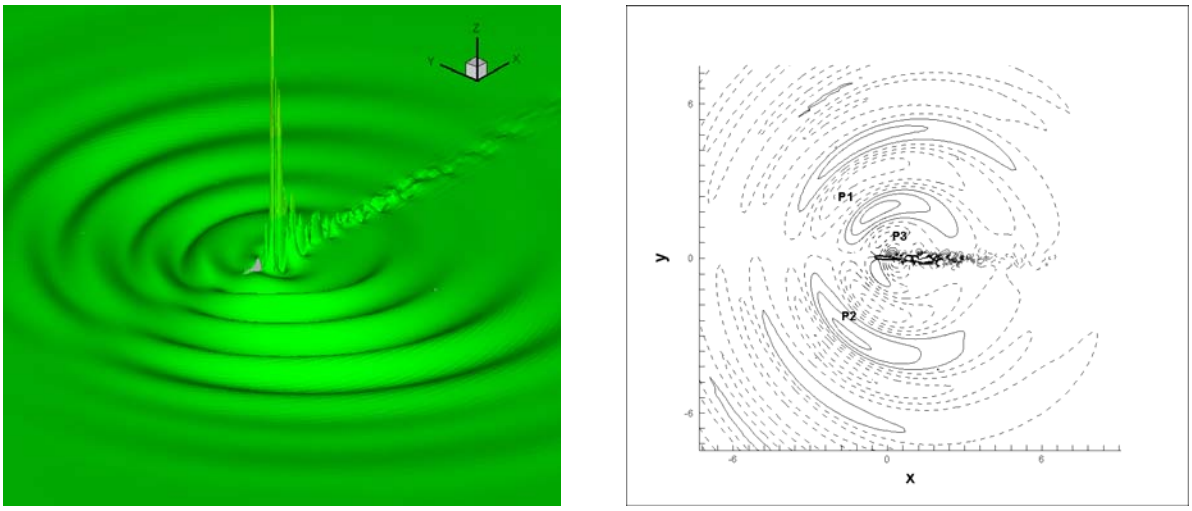

(a) (b)

Figure 4 (a) 3D view of the acoustic pressure waves for flow past a NACA 0012 airfoil at a Reynolds number 100 000, a Mach number of 0.2 and incident angle of 5°. (b) Contour plot of the acoustic pressure where P1, P2, P3 are three receiver points, pressure contour level is between ±0.015.

Both flow and acoustic simulations are done in a non-dimensional way, with the Reynolds number and the Mach number as input information and other quantities set equal to unit. Fourier transformation of acoustic signals are carried out at three receiver points and translated to the real dimensions. Assuming sound speed is known, e.g. 340m/s, the dimensional inflow speed U is known based on the given Mach number. The actual chord length is calculated with $c = Re \cdot v/U$. Finally, time is scaled with a factor U/c. The sound pressure level is found from

$$SPL = 20\log10(S / N / p_{const} \times 1.01 \times 10^5 / \sqrt{2} / p_{ref}), \quad (23)$$

where S is the magnitude obtained from Fourier transformation of the non-dimensional acoustic time history signal at a receiver point, N is the number of data points, p_{ref} = 2e-5 is the reference pressure for noise propagation in atmosphere and $p_{const} = \rho/(\gamma \cdot M_a^2)$ where γ indicates the specific heat ratio.

In Figure 5(a), it is seen that the spectrum are similar at all 3 receiver points P1, P2 and P3. The overall sound pressure levels at the 3 receiver points are 118 dB, 119 dB and 124 dB respectively. The sound pressure level at P3 is slightly higher since it is the point closest to the airfoil.

The lift and drag coefficient are also saved as time history data. In Figure 5(b), the noise spectrum at test point P3 is compared with the lift and drag spectra. The data are rescaled in order to gather them in the same figure. The lift and acoustic data are obtained by solving flow and acoustic equations individually, but their spectra are very similar which indicates the dependence between the force fluctuation and the sound generation. It is possible to see from Figure 5(b) that the energy distribution in the acoustic spectrum is very close to that in the lift spectrum particularly at those highest peaks. This proves that in this case the generation of noise is due to the lift force fluctuation on the body surface. According to the theories of Curle [2], turbulent flow produces fluctuating lift on solid bodies and should result in the generation of sound. It can be concluded that if the unsteady loading acting on a solid body is known as a function of time, the sound frequency components are also known. In the present case the drag force is rather small compared to the lift force, therefore the fluctuating lift is the dominant noise source.

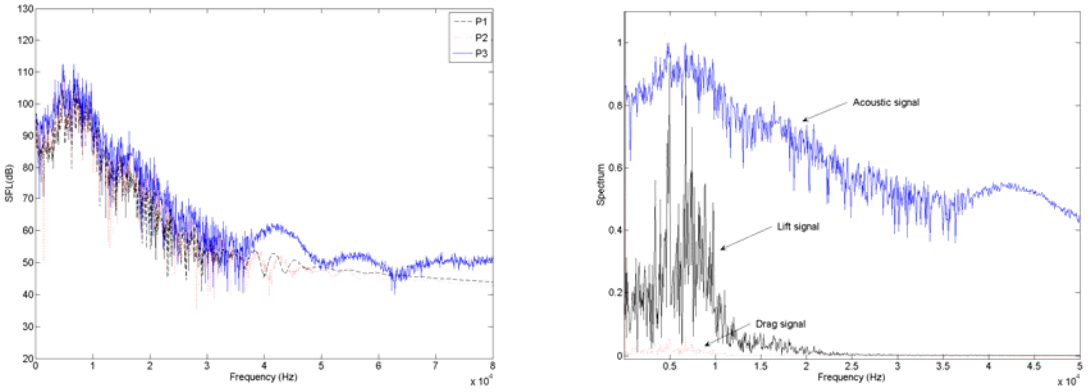

(a) (b)

Figure 5 (a) Computed broadband noise spectra at 3 receiver positions: P1, P2 and P3 that are marked in Figure 4(b). (b) Comparison of the non-dimensional noise spectrum with the lift and drag spectra.

5. Conclusions

A high-order numerical method for acoustic generation and propagation in the near field has been introduced. The simulations include incompressible flow and acoustic calculation. The flow part is solved with a second-order finite volume incompressible method with a SGS turbulence model. Either 4^{th}-order DRP or 6^{th}-order optimized compact finite difference schemes are applied for the aeroacoustic computations. At each time step, the incompressible variables are used as an input to the inviscid acoustic equations. The acoustic filed will not give any feed back to the flow field at low Mach number flows. The method is validated against a benchmark problem and applied for turbulent airfoil flow. At a Reynolds number of 10^5, the acoustic fluctuation has a strong dependence on the aerodynamic lift fluctuation on the airfoil surface. Therefore the energy distribution of an acoustic signal can be estimated by studying the fluctuating lift spectrum even without solving the acoustic equations.

References

[1] Lighthill M J 1952 On sound generated aerodynamically: I.General Theory. *Proceedings of the Royal Society of London, Series A (Mathematical and Physical Sciences)* **211** 564-587.
[2] Curle N 1955 The Influence of Solid Boundaries upon Aerodynamic Sound. *Proceedings of the Royal Society of London, Series A. Mathematical and Physical Sciences* **231** 505-514.
[3] Ffowcs Williams J E and Hawkings D L 1969 Sound generation by turbulence and surfaces in arbitrary motion. *Philosophical Transactions of the Royal Society of London A (Mathematical and Physical Sciences)* **264** 321-342.
[4] Hardin J C and Pope D S 1994 An acoustic/viscous splitting technique for computational aeroacoustics. *Theoret. Comput. Fluid Dynamics* **6** 321-42.
[5] Shen W Z and Sørensen J N 1999 Comment on the Aeroacoustic Formulation of Hardin and Pope. *AIAA J.* **1** 141-143.
[6] Shen W Z and Sørensen J N 2001Aero-acoustic modelling of turbulent airfoil flows. *AIAA J.* **39** 1057-1064.
[7] Shen W Z and Sørensen J N 2004 A collocated grid finite volume method for aeroacoustic computations of low-speed flow. *J. Comput. Phy.* **196** 348-366.
[8] Tam C K W and Webb J C 1993 Dispersion-Relation-Preserving finite difference schemes for computational acoustics. *J. Comput. Phy*. **107** 262-281.
[9] Lele S K 1992 Compact finite difference schemes with spectral-like resolution. *J. Comput. Phy*. **103** 16-42.
[10] Kim J W and Lee D J 1996 Optimized compact finite difference schemes with maximum

resolution. *AIAA J.* **34** 887-893.
[11] Carpenter M H, Gottlieb D and Abarbanel S 1993 The stability of numerical boundary treatments for compact high-order finite-difference schemes *J. Comput. Phy.* **108** 272-295.
[12] Bogey C and Bailly C 2004 A family of low dispersive and low dissipative explicit schemes for noise computations *J. Comput. Phys.* **194** 194–214.
[13] Tam C K W and Hardin J C (Eds.) 1997 Second Computational Aeroacoustics Workshop on Benchmark Problems NASA CP-3352.
[14] Michelsen J A 1992 Basis3D – A platform for development of multiblock PDE solvers. *Technical Report AFM 92-05. Technical University of Denmark.*
[15] Sørensen N N 1995 General purpose flow solver applied over hills. *RISØ-R-827-(EN) Risø National Laboratory, Roskilde Denmark.*